Lawrence Berkeley National Laboratory
Recent Work

Title
Electron Energy Loss Spectroscopy: Fundamentals and Applications in the Characterization of Minerals

Permalink
https://escholarship.org/uc/item/3fv3m5sq

Journal
Spectroscopic Characterization of Minerals and Their SurfacesACS Symposium Series, 415

Author
Krishnan, K.M.

Publication Date
1990

eScholarship.org Powered by the California Digital Library
University of California

LBL-26222 c.1

Lawrence Berkeley Laboratory

UNIVERSITY OF CALIFORNIA

Materials & Chemical Sciences Division

National Center for Electron Microscopy

RECEIVED
LAWRENCE
BERKELEY LABORATORY

FEB 15 1989

LIBRARY AND
DOCUMENTS SECTION

Presented at the American Chemical Society Meeting on Structures and Active Sites of Minerals, Los Angeles, CA, September 28–29, 1988, and to be published in the Proceedings

Electron Energy-Loss Spectroscopy: Fundamentals and Applications in the Characterization of Minerals

K.M. Krishnan

November 1988

TWO-WEEK LOAN COPY

This is a Library Circulating Copy which may be borrowed for two weeks.

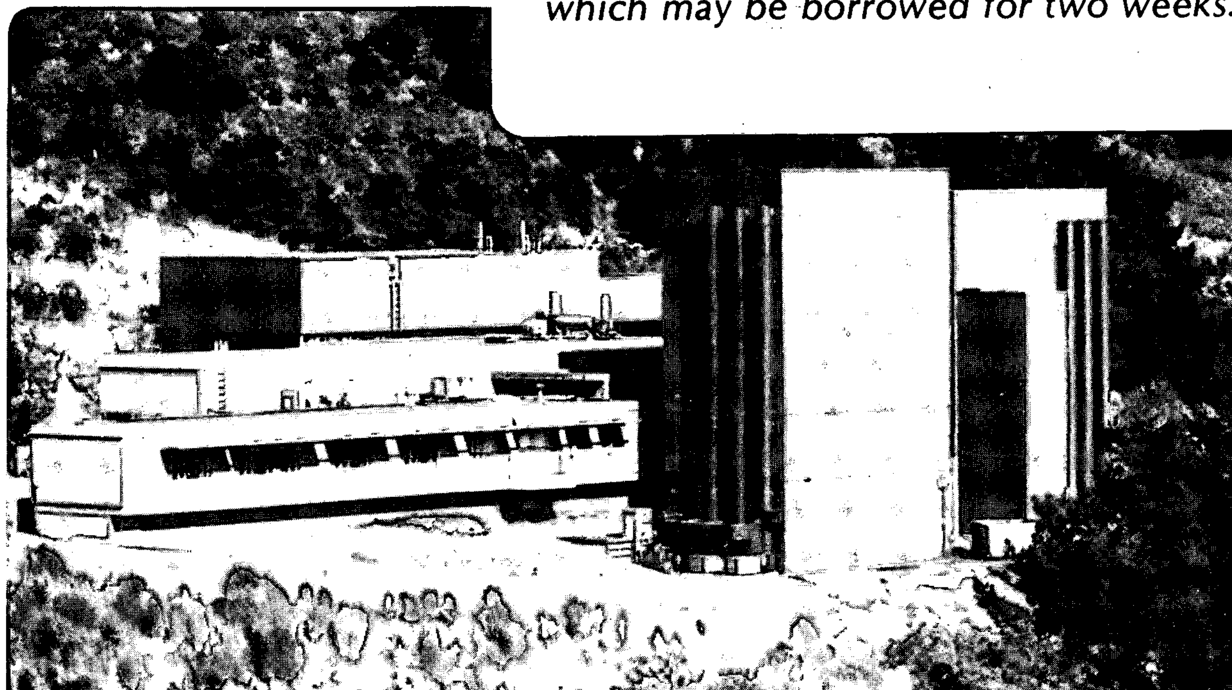

LBL-26222 c.1

Prepared for the U.S. Department of Energy under Contract Number DE-AC03-76SF00098.

DISCLAIMER

This document was prepared as an account of work sponsored by the United States Government. While this document is believed to contain correct information, neither the United States Government nor any agency thereof, nor the Regents of the University of California, nor any of their employees, makes any warranty, express or implied, or assumes any legal responsibility for the accuracy, completeness, or usefulness of any information, apparatus, product, or process disclosed, or represents that its use would not infringe privately owned rights. Reference herein to any specific commercial product, process, or service by its trade name, trademark, manufacturer, or otherwise, does not necessarily constitute or imply its endorsement, recommendation, or favoring by the United States Government or any agency thereof, or the Regents of the University of California. The views and opinions of authors expressed herein do not necessarily state or reflect those of the United States Government or any agency thereof or the Regents of the University of California.

ELECTRON ENERGY-LOSS SPECTROSCOPY: FUNDAMENTALS AND APPLICATIONS IN THE CHARACTERIZATION OF MINERALS

KANNAN M. KRISHNAN

National Center for Electron Microscopy
Materials and Chemical Sciences Division
Lawrence Berkeley Laboratory, Blg. 72
1 Cyclotron Road
Berkeley, California 94720
USA

Presented at the Annual Meeting of the American Chemical Society (Los Angeles, September, 1988) and to be published as a book chapter in the ACS publication entitled, "Structures and Active Sites of Minerals: Optical and Non-Optical Spectroscopic Characterization, (editors: L.M. Coyne, D.F. Blake and S. McKeever)."

Electron Energy-Loss Spectroscopy: Fundamentals and Applications in the Characterization of Minerals

Kannan M. Krishnan

National Center for Electron Microscopy, Materials and Chemicals Sciences Division, Lawrence Berkeley Laboratory, Blg. 72, Berkeley, CA. 94720

The combined use of an energy-loss spectrometer and an analytical electron microscope with fine probe forming capabilities provides a wealth of information about the sample at high spatial resolution. Fundamental principles governing the physics of the interaction between the fast electron and a thin foil sample, to account for the fine structure in the inelastically scattered fast electron distribution (EELS), will be reviewed. General application of EELS is in the area of low atomic number elements ($Z<11$) microanalysis, where it significantly complements the more widely used EDX spectroscopy. However, a careful analysis of the low loss plasmon oscillations and the fine structure in the core-loss edges, can provide additional information related to the bonding and electronic structure of the sample. An illustration of this is presented from our study of Cδ diamond residue from the Allende carbonaceous chondrite. Combination of EELS with channeling effects can provide specific site occupation/valence information in crystalline materials. Details of this novel crystallographic method will be outlined and illustrated with an example of the study of chromite spinels.

Finally, some pertinent experimental details will be discussed.

INTRODUCTION

The interaction of a fast electron, accelerated through kilovolt potentials in an electron microscope, with a thin foil will produce a variety of signals that can be monitored with appropriate detectors to provide a wealth of information about the crystallography, chemistry and electronic structure of the sample [1-3]. With the advent of improved electron-optics designs and high vacuum/voltage technologies it is increasingly possible to perform these microanalytical characterizations at high spatial resolutions. The crystallographic and structural information is contained in the elastically scattered beams and can be effectively interpreted either by the measurement of the electron diffraction patterns or by the recording of the diffraction contrast (conventional) and phase contrast (high resolution) images. On the other hand, the inelastically scattered fast electron intensity distribution and the multitude of emissions produced by the response of the sample to its excitation by the incident beam, incorporate the chemical and electronic structure information. In particular, the de-excitation processes are well understood and form the basis of an assortment of established analytical characterization methods in a TEM environment. These include x-ray emission spectroscopy (EDXS, WDS) [4], Auger electron spectroscopy [5] and cathodoluminescence [6]. However, it can be argued that, by the conservation of energy principles, all the above signals should have their counterparts in the inelastically scattered primary electron, provided its distribution as a function of energy or momentum (electron energy-loss spectroscopy) [7-9] can be monitored and interpreted. In this article the fundamentals and the current status of this technique, with some examples of its application to the characterization of minerals, is discussed.

FUNDAMENTALS OF ELECTRON ENERGY-LOSS SPECTROSCOPY

A representative EEL spectrum is shown in Figure 1 and can be broadly divided into three regions. The zero-loss peak (ZLP) consists of electrons that have traversed through the sample without interaction with its constituent atoms and emerging on the exit surface with the same energy as the primary beam. The full width at half maximum (FWHM) of the ZLP is a measure of the energy resolution of the experimental arrangement and is a function of both the energy spread of the primary beam (source) and the resolution of the spectrometer. It is fair to say that for currently available commercial spectrometers, under optimal operating conditions, the resolution is only limited by the thermal spread of the electron source and the abilities of the operator. The low-loss region [9] extending up to energy losses of ~100eV, consists of broad resonance peaks called plasmons representing the collective excitation of the delocalized outer-shell electrons by the primary beam. In a simple jellium or free-electron gas model [10] the plasmon energy is proportional to the square root of the number density of free electrons in the thin film [11]. The plasmon line-width is a function of the relaxation time required for the decay of the oscillation and is determined by the average grain size of the material; significant broadening due to grain boundary damping for small crystallite sizes (~6-7μm diameter) has been reported [12]. In thicker samples secondary plasmons at multiples of the primary plasmon energy, due to plural scattering, can be observed. In fact, a ratio of the ZLP to the total spectrum (ZLP + plasmons) is a simple well tested method of obtaining an estimate of the sample thickness [13]. In a TEM, EELS experiments are best performed at thicknesses where the plasmon is one tenth the height of the ZLP.

At higher energy losses, one observes edges corresponding to the interaction of the fast electron with the deeply bound core electrons of the sample. The onset of the edge generally corresponds to the ionization energy of the core electrons. As the binding

energies of the core electrons are a function of the atomic number, the position of the edges can be used to unequivocally identify the elements that constitute the sample. In addition, in the process of ejecting the core electron to the continuum, the fast electron can impart varying amounts of energy (up to a maximum of the primary energy minus the binding energy) to it. However, the probability of it doing so decreases with increasing energy-loss. Hence, the overall shape of an EELS core edge is a sharp onset followed by a smooth decay, (Figure 1b), which often results in significant edge overlap. Moreover, preceding edges can cause considerable backgrounds to edges at higher energy losses. The problem is sometimes compounded in thicker samples due to plural scattering. However, signal processing methods for the modelling of the background [14, 15, 7] and the deconvolution of multiply scattered spectrum [16,17] are well established. Alternatively, the core electron can be promoted from its initially well defined atomic orbital to a vacant state above the Fermi level (an unoccupied bound state in the conduction band or an empty antibonding molecular orbital level). The resulting near and extended fine structures observed above the ionization edge are hence a function of both the initial and final state wave functions of the excited electron and can provide information about the valence of the excited atom as well as its local chemical environment [7].

The inelastic electrons are scattered through relatively small angles when compared with the elastically scattered electrons, i.e., they are strongly forward peaked. In general, primary electrons that lose more energy tend to be scattered through larger angles. In practice this results in not all the energy-lost electrons being detected, as finite collection or entrance apertures to minimize electron-optical aberrations are used. Both the shape of the spectrum as well as the overall intensities (detection efficiency) are affected by these apertures.

When a small (<100 mrad) collection aperture is used, the predominant transitions observed in an energy-loss spectrum are the ones governed by the dipole selection rules. In that sense, EEL spectra are similar to x-ray absorption spectra and the optical

selection rules $\Delta l = \pm 1$ apply. Standard spectroscopic nomenclature is used to identify the core edges, ie., K (1s), L_1 (2s), L_2 ($2P_{1/2}$), L_3 ($2P_{3/2}$), M_1 (3s), M_2 ($3P_{1/2}$), M_3 ($3P_{3/2}$), M_4 ($3d_{3/2}$), M_5 ($3d_{5/2}$),..., etc. In practice, only a few of these transitions can be recorded with ease and the relevant edges are those corresponding to an initial state of maximum l for a given n [8]. Hence, transitions arising from 2p, 3d... initial states are an order of magnitude more intense than the 2s, 3s, 3p... contributions.

Three basic edge shapes (Figures 1a and b) are broadly observed. As the wave functions of the core electrons undergo very little change upon aggregation into a solid, a simple atomic model can predict their general shapes [19, 20]. They are: a) "saw tooth" profile, such as those calculated using hydrogen-like or Hartree-Slater wave functions for K-shell edges. Experimentally observed edges (O-K edge in Figure 1b) conform to this general shape but with some additional fine structure at the onset; b) "sleeping-whale" profile, a delayed maximum observed approximately 20 eV above the ionization edge, usually resulting from a large centrifugal barrier due to the l' (l' + 1) term in the radial Schrodinger equation. These are commonly observed for the $L_{2,3}$ edge of the third period elements Na-Ar (another typical example is the Ba $N_{4,5}$ edge in Figure 1a); c) "white lines" arising from distinct spin-orbit split levels, and typically observed in the $L_{2,3}$ edges of the fourth period elements (Cu $L_{2,3}$ edge in Figure 1b). $L_{2,3}$ edges probe the s- and d- symmetric portions of the final state wave functions. The latter can become large and narrow and can lead to sharp threshold peaks, particularly in a solid with a high density of unoccupied d states. The L_3/L_2 intensity ratio is often different from the statistical value of 2.0 based on initial state occupancy and can be used to determine the oxidation state [21].

Superimposed on the broad edge shapes are the fine structures due to solid state effects. At the edge threshold one can measure a displacement of the onset or "chemical shift". In EELS, the ionization edge threshold is a function of both the initial state as well as the position and nature of the vacant states at the Fermi level. Band structure effects such as band gaps can be easily resolved (example:

diamond C 1s -> σ^* = 288 eV, graphite C 1s -> π^* = 284 eV). In addition, positive chemical shifts are also observed with increasing oxidation states [22] because oxidation removes valence electrons, leads to reduced screening of the nuclear field and a deepening of the potential well (of the initial state). The near edge fine structures (ELNES) observed ~5-50 eV above the ionization edge can be interpreted, in the first approximation, using a simple one electron transition model between the initial state and a vacant final state in the conduction band:

$$I(E) \propto T(E)\ N(E) \qquad (1)$$

where T(E), the transition probability, is a slowly varying function of energy loss and N(E) is the density of final states. This simple model is a reasonable basis for the interpretation of ELNES, provided N(E) is defined, as and when required, to include the following ideas (a) dipole selection rules apply, i.e., N(E) is interpreted as a symmetry projected density of states clearly distinguishing the K and L edges; (b) core-level states are highly localized - N(E) is a local density of states determined for that particular lattice site and reflecting the local symmetry [23]; (c) N(E) is in reality a joint density of initial and final states and broadening based on the lifetimes of both the core hole and the final states is incorporated.

Finally, extended fine structure (EXELFS) is also observed as weak oscillations superimposed on the high-energy tail of a core loss spectrum [49]. This is interpreted as a density of states phenomenon, involving scattering of the ejected core electron by the nearest neighbour atoms. Hence, this is a measure of the short range order and provides information regarding nearest neighbour distances and coordination number, provided sufficient counts can be accumulated to make a statistically significant analysis.

FINE STRUCTURE ANALYSIS: TWO EXAMPLES IN THE CHARACTERIZATION OF MINERALS

CΔ RESIDUE FROM ALLENDE. Cδ diamond residues, obtained by an acid and oxidant treatment of fragments of the Allende CV3 meteorite were extensively characterized by a variety of electron-optical methods [24, 25, 26] Microdiffraction patterns obtained from nanometer scale residue particles using 10 nm probes confirmed that these particles were indeed diamond with a lattice parameter of 0.365 nm - an expansion of ~2% from the ideal structure These diamond residues, along with diamond films recently produced by a low pressure CVD method [27] were characterized by EELS. Both the low-loss plasmon excitations as well as the fine structure in the core-loss edges were measured and interpreted. The low-loss spectra (Figure 2) show that both materials exhibit characteristic bulk diamond plasmon resonances at ~30-34 eV. However, the LPCVD diamond film exhibits a distinct shoulder at 24 eV, a feature that was found to be thickness dependent. Since the EELS were measured for a 20-25 nm thick sample, it was concluded that this feature was a result of surface hydrocarbon contamination. No such shoulder was observed for the Cδ residue - the sample surface was very clean. The only significant difference was a broadening of the plasmon half-width. However, the degree of broadening was consistent with the grain boundary damping for 5-10nm crystallites [12].

The C-K edges for the LPCVD and Cδ diamonds are shown in Figure 3. The onset of the edge, and the fine structure of the core edge for the LPCVD diamond, including the good agreement with a calculated density of unoccupied states, corresponds to the ls -> σ^* transition in the sp^3 hybridized carbon in diamond. In the case of the Cδ residue one additional π^* feature normally associated with the 1s -> π^* transition in graphite is observed at 286.8 eV. The analysis of the plasmons resonance data, mentioned earlier, indicated no surface contamination. Hence, the C 1s -> π^* transition observed has

been attributed to the presence of sp^2 carbon on the surface/interface of nanometer scale diamond residue. In fact, a good match was obtained between the experimentally observed spectrum and an artificial spectrum of 25% sp^2 and 75% sp^3 carbon. In practice, this could easily be achieved if each 10 nm diameter particle were to have 6-8 monolayers of sp^2 carbon surrounding it. The accompanying relaxation to accommodate the elastic strains resulting from the topological reconstruction caused by the π bonding on the surface of each particle, as has been reported [28] for the (100) diamond surface, would be in agreement with the 2% increase in lattice parameter measured by the microdiffraction experiment.

DETERMINATION OF THE OXIDATION STATES OF THE 4th PERIOD TRANSITION METALS IN MINERALS. The study of the oxidation states of polyvalent cation is an important component of the characterization of minerals as they not only have vital crystal-chemical implications, but are also useful monitors of the ambient oxygen fugacities [21]. The techniques conventionally employed for the determination of the oxidation states, such as Mössbauer, optical and x-ray absorption, etc., have limited applicability because of the difficulty in obtaining a sufficiently pure amount of the fine grained or inhomogenous mineral sample. EELS avoids many of these difficulties, particularly when combined with the fine probe forming capabilities of an analytical electron microscope.

The $L_{2,3}$ edges of the 4th period transition metals are marked by prominent "white line" features due to excitations of the $2p_{3/2}$ (L_3) and $2p_{1/2}$ (L_2) levels, following the allowed dipole transitions, to unoccupied d states. On the basis of the (2j + 1) degeneracy in a one electron model, the L_3/L_2 intensity ratio should be 2:1, but wide departures from this ratio have been observed in transition metals and their oxides [21, 22, 29, 30]. Even though no single factor has been found to account for these observations, these extensive studies form the basis of an empirical catalogue of L_3/L_2 ratios to be used in future determinations of the oxidation states. Further, positive chemical shifts are also observed as a function of oxidation states for Ti^{3+} - Ti^{4+} (2 eV), Mn^{2+} - Mn^{4+} (2 eV), Fe^{2+} - Fe^{3+} (2 eV), etc. [21],

for the reasons mentioned earlier. A typical example for manganese is shown in Figure 4. A 2 eV chemical shift in the L_3 peak is observed between Mn^{2+} and Mn^{4+}. The L_2/L_3 ratio changes from 0.25 (MnO) to 0.65 (MnO_2). However, there are some difficulties in performing these experiments, especially in minerals containing mixed valence states, due to the strong overlaps between edges of different oxidation states.

MICROANALYSIS

In addition to the study of fine structures in EELS to obtain bonding and chemical information, this spectroscopic method is being increasingly used for quantitative microanalysis. In particular, the emphasis has been on light element ($Z < 11$) quantification, a domain in which this method compliments (and often has significant advantages over) the more commonly used EDXS. For a sample that is sufficiently thin (~30-60nm thick), the procedure is simple and straightforward and involves the measurement of the area under the appropriate ionization edge after background subtraction. However, the detection of hydrogen in a solid is complicated because the H^{1s} electron is involved in the solid state orbitals and the K-edge at 13.6 eV is obscured. It is not certain whether its electron (in a metallic lattice, say) is retained by the hydrogen nucleus or it is transferred to the conduction band, resulting in a shift of the host Fermi level. In fact, shifts in the plasmon energy in hydrides have been observed, and these shifts have been interpreted in terms of the composition in a variety of systems [31, 32]. This approach is difficult, involves an understanding of the modification of the band structure due to the addition of hydrogen, and often leads to detection limits orders of magnitude worse [8] than the simple EELS microanalysis formulation for $Z>3$.

In a typical EEL spectrum, the count rate I_A (area under the excitation edge after background subtraction, for element A) is a product of the incident electron current density, J_o, the number of atoms N_A of element A per unit area, and σ_A, the total ionization cross-section per atom for the excitation of the appropriate inner-

shell by the incident electrons. However, to preserve good energy resolution, an aperture is placed after the specimen which limits scattering to angles less than β and hence only a fraction of the core loss signal $I_A(\beta)$ is measured. Moreover, in most microanalytical situations $I_A(\beta)$ is superimposed on a strong background and this problem combined with that of edge overlap is best avoided by measuring $I_A(\beta, \Delta)$ over a limited energy-loss range, Δ following the ionization edge E_A. Hence, the absolute concentration of atoms, N_A is given by [34].

$$N_A = [J_o(\beta,\Delta) \quad \sigma_A(\beta,\Delta)]^{-1} \quad I_A(\beta, \Delta) \tag{2}$$

where $J_o(\beta,\Delta)$ is the total intensity measured with the aperture β for energy losses less than Δ, $\sigma_A(\beta,\Delta)$ is the partial ionization cross-section corresponding to a scattering angle of β and inner-shell losses between E_A and $E_{A+\Delta}$, and all relevant experimental quantities are shown in Figure 1b. $J_o(\beta, \Delta)$ can be substituted with I_o, the area under the zero-loss peak, if plural inelastic scattering can be corrected for by using appropriate deconvolution procedures [8, 34]. If only relative abundances of two elements A and B are required, then equation 2 becomes

$$\frac{N_A}{N_B} = \frac{I_A(\beta, \Delta)}{I_B(\beta, \Delta)} \; \frac{\sigma_B(\beta, \Delta)}{\sigma_A(\beta, \Delta)} \tag{3}$$

provided the data for the two edges are measured under identical experimental conditions of illumination, specimen thickness and scattering angles. The accuracy of quantitative analysis using this formulation is largely determined by the errors arising from the removal of the background below the ionization edge and the accuracy of the calculated (or experimental) ionization cross-sections.

Based on empirical observations, an inverse power law function of the form $I = AE^{-r}$, where the exponent r takes values 2-6 is now commonly used for the background [7]; even though there is no

physical basis for it [35]. A background fitting region immediately preceding the ionization region is chosen, the constants A and r determined by least squares refinement and the background extrapolated beyond the ionization edge for the required energy window Δ (Figure 1b). Errors can be introduced in the extrapolation procedure due to the statistics of the data in the fitting region and, more significantly, due to a systematic variation of the exponent 'r' with energy loss. In fact, in a recent study [15, 36] using a wide assortment of standards it has been shown that $r \propto \ln(E)$ and hence a polynominal fit [37] to the log-log spectrum gives a more satisfactory (minimizes extrapolation error) fit to the background. Alternatively, the use of library edges scaled to experimental data seems to show some promise, particularly for overlapping edges [38].

Two methods of calculating partial ionization cross-sections are currently in use. An approximate but easily programmable model, SIGMAK, for K shell edges based on hydrogen-like wave functions and scaled to account for the nuclear charge along with a screening constant independent of Z, has shown good agreement with experimental measurements [39]. For L-shells, (SIGMAL [40]), an additional empirical factor is introduced to match experimental data as the simple treatment for screening is inadequate [34]. Alternatively, the cross-sections can be calculated more accurately, using Hartee-Slater (HS) wave functions [20, 41], assuming that the element is in atomic form, neglecting solid state or excitonic affects and not including dynamic processes. Good agreement between the two theoretical methods is obtained for K edges, the only difference being the presence of sharp threshold peaks in the HS spectra. In the predictions of partial ionization cross-sections, both methods agree to within 5% for K edges and ~10% for L-edges. For the transition metal $L_{2,3}$ edges, both methods do not incorporate the "white lines" arising from the transition to the continuum d states. However, it is clear that their effect on microanalysis can be averaged out by using large (>100 eV) integration windows. In the SIGMAL program, an additional empirical parameter to deal with the white lines can be introduced [34]. Further, it is necessary to incorporate relativistic

kinematics in the calculations, particularly at the increasingly common medium (≥200 kV) operating voltages [42].

Alternatively, one can measure these ionization cross-sections and use them in much the same way as k-factors [43] are used in EDX microanalysis. Two systematic measurements, one for K, L edges [44] and the other for $M_{4,5}$ edges [45] are reported in the literature. However, experimentally measured cross-sections show large variations [34]. To overcome these difficulties, it is necessary to prepare standards of well known stoichiometry and to measure their thickness accurately. Finally, some of the measurements reported in the literature [33] have been made with large collection angles (~100 mrad) and should be used with caution as they could be erroneous due to lens aberration effects.

In summary, the overall error in microanalysis using EELS is a combination of the statistical error in the measurement of $I_A(\beta, \Delta)$ which for Poisson statistics (applicable in the case of EELS) is given by $\sqrt{I_A}$, the errors in background fitting and extrapolation (~5%), and the accuracy of the ionization cross-sections (theory: ~5-15%, experiments: ~2-5%).

Concepts of minimum detectable mass (MDM) and minimum detectable mass function (MMF) prevalent in EDXS quantification have also been defined for EELS microanalysis [46]. It suffices to say that utilizing current technology, MDM $\leq 10^{-20}$ gms. In fact, in a study of Uranium clusters using $O_{4,5}$ edges, a practical MDM of ~10 atoms, i.e., 10^{-20} gms, was measured [47]. However, in most practical situations these limits are generally determined by the migration of the atoms and their propensity to suffer radiation damage under the intense electron beam [48]. These effects need more thorough investigation, particularly in materials science and mineralogy applications.

ATOMIC SITE AND SPECIES DETERMINATION USING CHANNELING AND RELATED EFFECTS

For crystalline or microcrystalline materials both the characteristic energy-loss edges and the x-ray emission peak intensities show strong dependence on the orientation of the incident beam as they are governed by phenomena that are highly localized at the atomic sites. In general, an incident plane wave of electrons under strong dynamical diffraction conditions (Kikuchi lines visible in the diffraction pattern) sets up a standing wave within the crystal. For certain incident beam orientation, the standing wave modulation across the unit cell is such that its maximum coincides with a particular crystallographic site containing a specific atomic species and producing an enhancement of the corresponding characteristic energy-loss edge or x-ray emission peak intensities. Whilst these orientation dependencies could have detrimental consequences on EDXS/EELS microanalysis (and should be avoided either by selecting a non-channeling orientation where no lower order Bragg diffraction vectors are excited or by using a large convergence angle to average out the orientation dependence), they have been developed into a powerful crystallographic technique for specific site occupancy/ valence determinations [50, 51]. Either axial [52] or planar [53, 54] channeling orientations are used. For brevity, only the latter will be discussed here and the principles of the technique illustrated with our measurements for the dolomite structure.

The dolomite structure in the [1210] orientation, with the c-axis exaggerated for clarity, is shown in Figure 5. For a (0001) systematic row (a single row of spots in the diffraction pattern), the wave field of the dynamically diffracted electrons in the crystal is two-dimensional, i.e., constant in a direction normal to the c-axis. In the domomite structure, the candidate sites of interest (Mg and Ca) occupy alternating planes at one third the unit cell parameter along the c-axis. For the (0001) systematic row, at orientations corresponding to small positive excitation errors ($s>o$) (Figure 6) of the third order Bragg diffraction condition (3g) an enhancement of the Mg Kα is observed. For negative excitation errors ($s<o$) an

enhancement of the Ca Kα is observed. It can also be seen that the impurity Fe Kα intensity, follows that of Mg Kα, suggesting similar site occupancy. The exact degree of substitution of the impurity atoms (Fe) can be obtained by an elegant method of ratios [53] with respect to the intensities of the reference elements (Mg & Ca) in the host lattice. Site occupancies in a variety of minerals have been measured using this technique [55-57].

In the case of EELS, within the single scattering regime, applying the principle of reciprocity it can be shown that the intensities for different sites can be effectively squared by choosing the position of the detection aperture and placing it at an appropriate part of the diffraction pattern [58]. Further, from a simple application of the uncertainty principle ($\Delta x \cdot \Delta p \geq h$), considerable enhancement of the localization of the inelastic scattering event can be achieved by analyzing electrons scattered over large angles (or large momentum transfer). In practice, this is achieved by shifting the detection apertures parallel to the Kikuchi band (i.e., the (400) band in Figure 7a for the spinel structure) but without any change in the diffraction geometry with respect to the (400) planes. Significant enhancement, even for losses as low as 532 eV (O-K edge), can be achieved by promoting localization in this manner.

An example [59] for chromite spinels, where the EEL spectra are measured at different incident beam orientations and under strong localization conditions, is shown in Figure 7a. For orientation (a) the octahedral sites were selectively enhanced. For orientation (b) the tetrahedral sites are selected. However, because of the superior energy resolution of EELS (~1 eV), it is possible also to detect changes in oxidation states by the small chemical shifts observed in the onset of the core-loss edges. Combining this chemical shift with the selective enhancement of the different candidate sites by the appropriate choice of incident beam orientations, it is possible to obtain specific site valence information (Figure 7b). For example, a 2 eV chemical shift is observed between Fe^{2+} and Fe^{3+}. The higher energy Fe^{3+} peak intensity is enhanced when the incident electron beam is localized on the octahedral sites, while the Fe^{2+} intensity

variation with orientation suggests it occupies only tetrahedral sites in the naturally occurring chromite spiral.

EXPERIMENTAL DETAILS

The discussion is restricted to energy-analyzing devices compatible with analytical electron microscopes. Generally, they are either electrostatic or magnetic prisms placed after the specimen and the most popular commercial spectrometers are based on a magnetic sector design [60]. The principle of operation is quite simple. In a uniform magnetic field, fast electrons have circular paths, the radius of which is a function of both the incident electron energy and the strength of the magnetic field. Therefore, electrons of varying energy entering normal to the field can be brought to a focus at a specific exit point by suitably varying the strength of the magnetic field. However, if the incidence is not normal but over a finite angular range (in practice, defined by β) electrons of the same energy entering a constant magnetic field are spatially separated at the exit phase. Even though the aberration is normally compensated for in the design of the spectrometer, it is impossible to avoid the relationship between the energy resolution and the entrance aperture of the spectrometer; i.e., the smaller the entrance aperture, the better the energy resolution. On the other hand, the collection efficiency (fraction of electrons losing energy E and scattered through β when compared to electrons scattered through all possible angles) is inversely proportional to β and E. Hence, one gains energy resolution invariably at the expense of collection efficiency.

The spectrum (dispersion of electrons losing varying amounts of energy) is formed along a straight line in the back focal plane of the spectrometer and is recorded in one of two ways. Until recently, a serial mode in which a narrow energy range is recorded at any particular moment using a set of post-spectrometer selection slits or apertures, was the norm. The spectrum was swept past the narrow slits generally by ramping the current in the magnet and thus the magnetic field. This has an inherently low collection efficiency

magnetic field. This has an inherently low collection efficiency (~0.01), because only a small fraction of the spectrum is acquired at any particular time. A typical EEL spectrum has intensities that vary over eight decades of counts and the major advantage of such a system is its dynamic range which can accommodate this variation in signal magnitude. However, a parallel recording system (PEELS) which uses a set of quadrapole lenses to magnify the spectrum in such a manner that it can be simultaneously recorded by a single crystal YAG scintillator coupled to a 1024-channel photodiode array, is now commercially available [61]. This system has been shown to achieve much higher efficiencies (>0.25) over the range of intensities relevant to EELS in a TEM. Routine use of such a PEELS requires that the "dark characteristics" (i.e., no incident electrons) of the array under identical conditions of acquisition as the spectrum of interest be recorded and subtracted from it. Moreover, the response of the individual elements of the photodiode array to the same signal could vary from one to the other and this has to be measured by ramping a constant signal (such as the zero loss peak) across the array in much the same way as in serial detection. The spectrum should then be divided by the "channel to channel gain variation" measured in this fashion to avoid any artefacts. Finally, as the individual elements of the detector saturate at 2^{14} (16384) counts, recording of the ZLP and the low-loss region can be accomplished only in a separate acquisition using very low incident electron illumination and very small acquisition times. This often leads to problems if thin specimens cannot be prepared. In such cases, it is essential to deconvolute the spectrum to eliminate plural scattering and obtain a single scattered distribution. All well established deconvolution procedures [16, 17] require that the low-loss region, including the ZLP, be acquired under identical conditions as the core-loss feature of interest.

Generally any sample that is suitable for high resolution electron microscopy would also be appropriate for EELS. Increasing the sample thickness would, in principle, increase the signal of interest (linear), increase the probability of multiple scattering and increase the probability of mixed (elastic and inelastic, etc.) events.

While the first consequence is desired, the latter two are clearly detrimental. Ultimately, there is no substitute to having a uniformly thin specimen whose thickness optimally [62] would be less than one mean free path length for total inelastic scattering (λ_p). λ_p is proportional to the mean atomic number of the sample and has been recently parameterized [13]. If one is constrained by a lower limit of specimen thickness, an option would be to go to higher acceleration voltages as λ_p would increase linearly with kV. Alternatively, if one is performing an EELS experiment with an optimally thin sample but is interested in the characteristic signal from an element occurring in very small quantities, it is possible to enhance the signal by selecting a larger area and operating in diffraction mode. But if higher spatial resolution is also required there is no option but to use a high current density source, such as a field emission gun. However, such sources should be used with caution [48] as they can cause significant radiation damage, including loss in long range order, breaking of bonds and in some cases, outright vapourization of the sample. On the positive side, it is currently accepted that retaining the sample at cryogenic temperatures can alleviate some of these problems, but to what extent is yet to be determined.

ACKNOWLEDGMENTS

This work was supported by the Director, Office of Energy Research, Office of Basic Energy Sciences, Materials Sciences Division, of the United States Department of Energy under contract No. DE-AC03-76SF00098. The author would like to thank Dr. R. Kilaas for a critical reading of the manuscript.

LITERATURE CITED

1. P.B. Hirsch, A. Howie, R.. Nicholson, D. Pashley, and M.J. Whelan, Electron Microscopy of Thin Crystals, (Butterworths, London), 1965.
2. J.J. Hren, J.I. Goldstein and D.C. Joy, Introduction to Analytica Electron Microscopy. (Plenum, New York), 1979.

3. J.M. Cowley, Diffraction Physics, (North Holland, Amsterdam), 1981.
4. S.J.B. Reid, Electron Microprobe Analysis, (Cambridge Univ. Press), U.K.), 1975.
5. M.P. Seah, SEM/II, **521** (1983).
6. B.G. Yacobi and D.B. Holt, J. Appl. Phys., 59 R1 (1986).
7. R.F. Egerton, EELS in the Electron Microscope, (Plenum, New York), 1986.
8. C. Colliex, in Advances in Optical and Electron Microscopy, ed. V.E. Cosslett and R. Bauer, (Academic, London), **9**, 65 (1984).
9. H. Raether, Excitations of Plamons and Interband Transitions by Electrons, (Springer-Verlag, Berlin), 1980.
10. D. Pines, Elementary Excitation in Solids, Benjamin, New York, (1963).
11. K.M. Krishnan, in Analytical Electron Microscopy, ed. D.C. Joy, San Francisco, 261 (1987)
12. C. von Festerberg, Z. Phys., **207**, 47 (1967).
13. R.F. Egerton, S.C. Cheng and T. Malis, Proc. EMSA, **45**, 122 (1987).
14. P. Trebbia, Ultramicroscopy, **24** 399 (1988).
15. K.M. Krishnan and M.T. Stampfer, Proc. EMSA, **46**, 538 (1988).
16. R.F. Egerton, B.G. Williams, D.T.G. Sparrow, Proc. Roy. Soc. Lond., **A398**, 395 (1985).
17. C.R. Swyt and R.D. Leapman, in Microbeam Analysis, ed. A.D. Romig and J.I Goldstein, S.F. Press, 45 (1984).
18. R.D. Leapman, et al. in EXAFS Spectroscopy, ed. B.K. Teo and D.C. Joy, Plenum Press, New York, 217 (1981).
19. S.T. Manson, Phys. Rev., **A6**, 1013 (1972).
20. R.D. Leapman, P. Rez and D.F. Mayers, J. Chem. Phys., **72**, 1232 (1980).
21. M.T. Otten et al., Ultramicroscopy, **18**, 285 (1985).
22. J.H. Rask, B.A. Miner and P.R. Buseck, Ultramicroscopy, **21**, 321 (1987).
23. J. Tafto and J. Zhu, Ultramicroscopy, **9**, 349 (1982).
24. R.S. Lewis, et al., Nature, **326**, 160 (1987).
25. D.F. Blake et al., Nature, **332**, 611 (1988).

26. D.F. Blake, F. Freund and K.M. Krishnan, Earth & Planetary Science Letters, in press.
27. J.C. Angus and C.C. Hayman, Science, **241**, 913 (1988).
28. D. Vanderbilt and S.G. Louis, Phys. Rev., **B30**, 6118 (1984).
29. T.G. Sparrow, et al., Chem. Phys. Lett., **108**, 547 (1984).
30. R.D. Leapman, L.A. Grunes and P.L. Fejes, Phys. Rev., **B26**, 614 (1982).
31. A.P. Stephens and L.M. Brown, Inst. Phys. Conf. Ser., **52**, 341 (1980).
32. N.J. Zaluzec, T. Schober and D.G. Westlake, Proc. EMSA, **39**, 194 (1981).
33. C.C. Ahn and O.L. Krivanek, EELS Atlas, ASU Tempe, AZ. (1983).
34. R.F. Egerton, SEM/II, 505 (1984).
35. M. Isaacson, Proc. XI Int. Cong. Elec. Mic., Kyoto, Japan, 37 (1986).
36. K.M. Krishnan, unpublished data.
37. J. Bentley, G.L. Lehman and P.S. Sklad, Electron Micrscopy, **1**, 585 (1982).
38. N.J. Zaluzec, Conf. Proc. Analytical Electron Microscopy, ed. R.H. Geiss, S.F. Press, San Francisco, 193 (1981).
39. R.F. Egerton, Ultramicroscopy, **4**, 169 (1979).
40. R.F. Egerton, Proc. EMSA, **39**, 198 (1981).
41. C.C. Ahn and P. Rez, Ultramicroscopy, **17**, 105 (1985).
42. M.M. Disko and R. Ayer, in Inter. Voltage Electron Microscopy, K. Rajan ed., Elec. Opt. Publ. Group, N.J., 72 (1988).
43. K.M. Krishnan, and C.J. Echer, Analytical Electron Microscopy, D.C. Joy ed., S.F. Press, 99 (1987).
44. T. Malis, K. Rajan, J.M. Titchmarsh, and C. Weatherly, Voltage Electron Microscopy, K. Rajan ed., 78 (1987).
45. P. Hofer, P. Golob, and A. Brunegger, AEM-Workshop, UMIST, Manchester (1987).
46. M. Isaacson and D. Johnson, Ultramicroscopy, **1**, 33 (1975).
47. C. Colliex, O.L. Krivanek and P. Trebbia, Inst. Phys. Conf., Ser., **61**, 183 (1981).
48. L.E. Thomas, Ultramicroscopy, **9**, 311 (1982).

49. S. Csillag, D.E. Johnson and E.A. Stern, Analytical Electron Microscopy, ed. R.H. Geiss, 221 (1981).
50. K.M. Krishnan, Ultramicroscopy, **24**, 125 (1988).
51. J. Tafto, J. Appl. Cryst., **15**, 378 (1982).
52. S.J. Pennycook and J. Narayan, Phys. Rev. Lett., **54**, 1543 (1985).
53. J.C.H. Spence and J. Tafto, J. Microscopy, **130**, 147 (1983).
54. K.M. Krishnan, P. Rez and G. Thomas, Acta Cryst., **B41**, 396 (1985).
55. P.G. Self and P.R. Buseck, Phil. Mag., **A48**, L21 (1983).
56. J. Taft and P.R. Buseck, Amer. Mineral., **68**, 944 (1983).
57. M.T. Otten and P.R. Buseck, Ultramicroscopy, **23**, 151 (1987).
58. J. Taft and O.L. Krivanek, Nucl. Inst. Methods, **194**, 153 (1982).
59. J. Taft and O.L. Krivanek, Phys. Rev. Lett., **48**, 560 (1982).
60. H.T. Pearce-Percy, SEM/I, 41 (1978).
61. O.L. Krivanek, C.C. Ahn and R.B. Keeney, Ultramicroscopy, **22**, 103 (1987).
62. M. Isaacson, SEM/I, 763 (1981).

FIGURE CAPTIONS

1. Electron energy-loss spectrum of $GdBa_2Cu_3O_{7+\delta}$ illustrating the various observable types of fine structures; a) the low-loss segment including the outer shell ionization edges; b) the inner shell core-loss edges; the background model AE^{-r} and the parameters used in microanalysis (I_A, E_A, Δ) are also shown.

2. The low-loss plasmon spectrum of a) low pressure chemical vapour deposition diamond films; b) diamond residue from the Allende carbonacious chondrite.

3. The fine structure of the C-K edges for the two types of diamonds studied. The fine trace is the unprocessed data and the points represent the deconvoluted single scattered distribution.

4. The $L_{2,3}$ edges for the Mn^{2+} and the Mn^{4+} illustrating both the chemical shift (2 eV) and the changes in L_3/L_2 intensity ratios.

5. Crystal structure of Dolomite in the [1210] orientation.

6. An example of the dependence of characteristic x-ray emissions on incident beam orientation for the dolomite structure.

7a. EEL spectrum of a chromite spiral under different incident beam orientations showing enhancement for the octahedral (a) and tetrahedral (b) sites. The position of the detection aperture to achieve enhanced localization for the low energy O-K edges is shown in the insert.

7b. Details of the Fe $L_{2,3}$ edge for the same orientations.

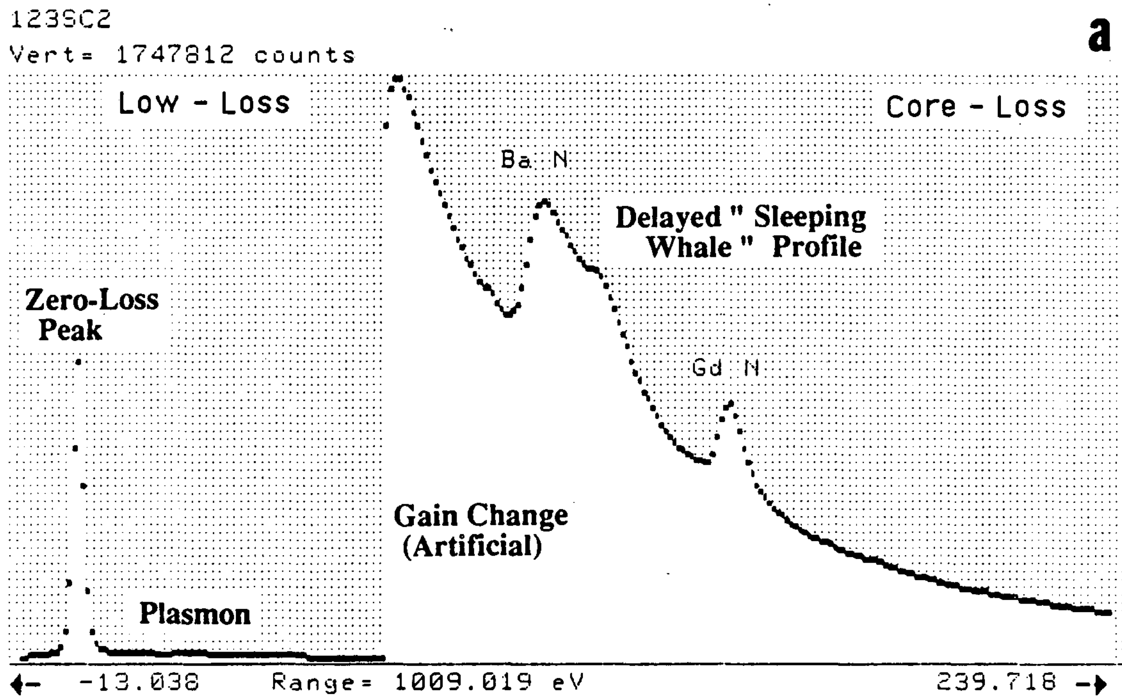

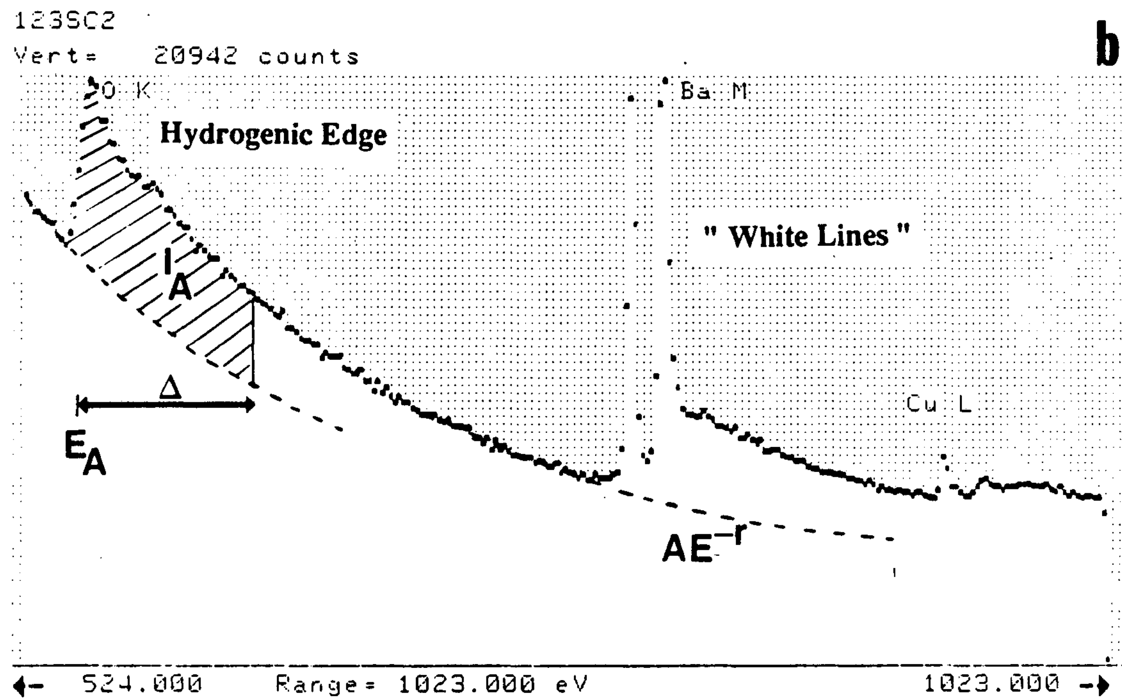

XBL 8810-3585

Figure 1

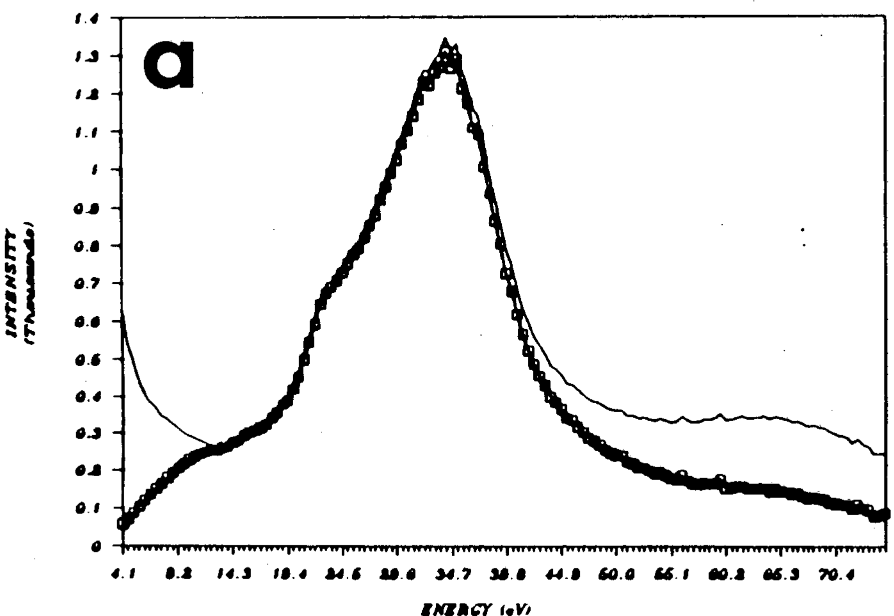

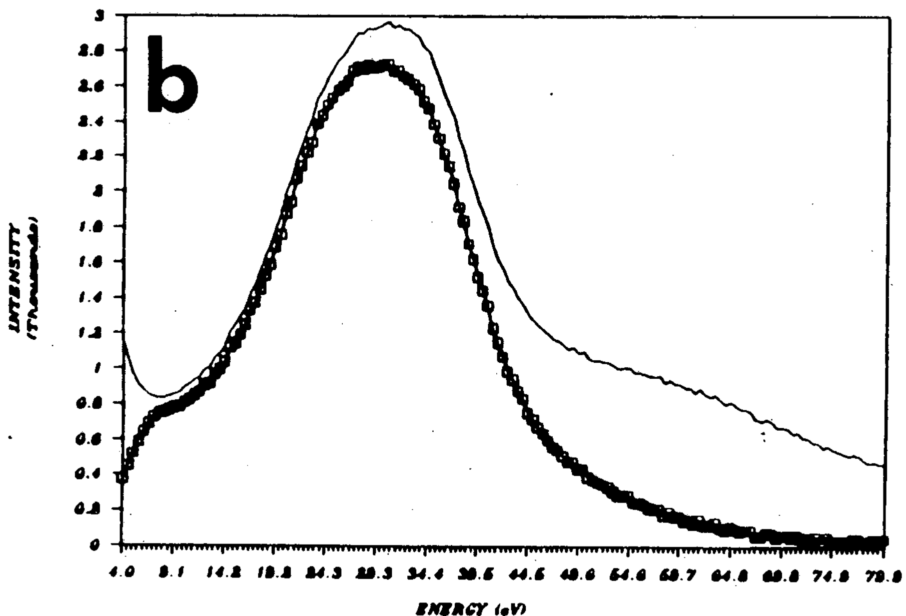

XBL 883-1003 A

Figure 2

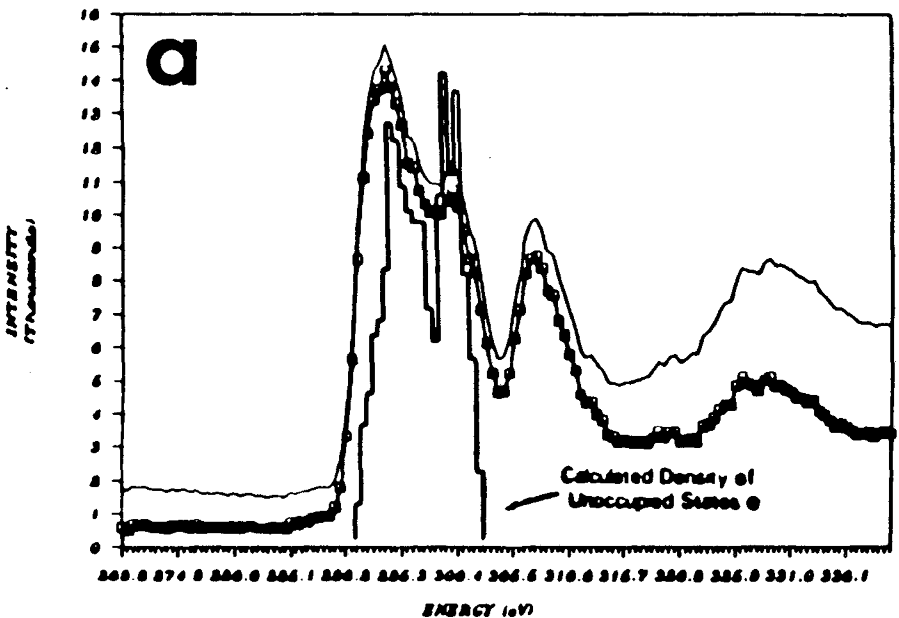

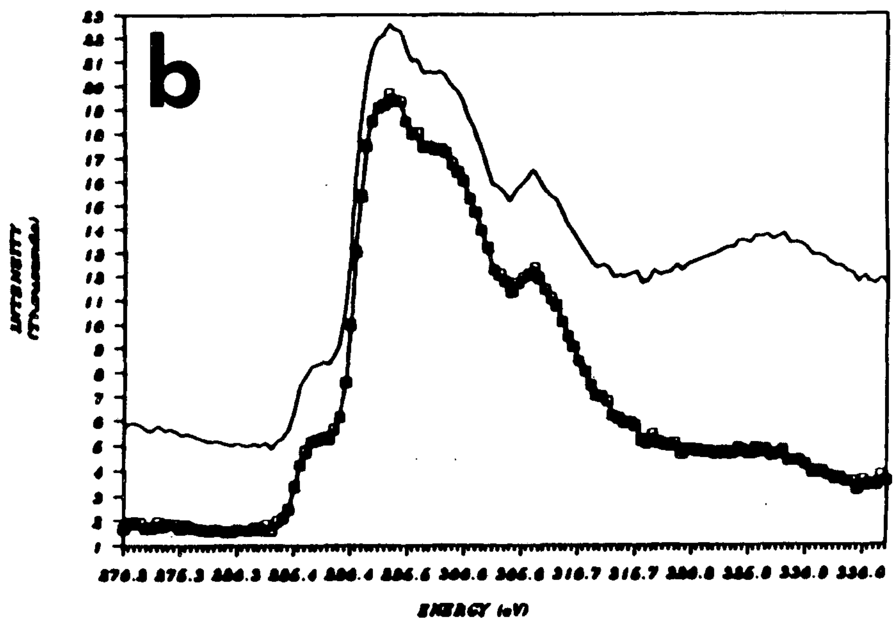

XBL 883-1002 A

Figure 3

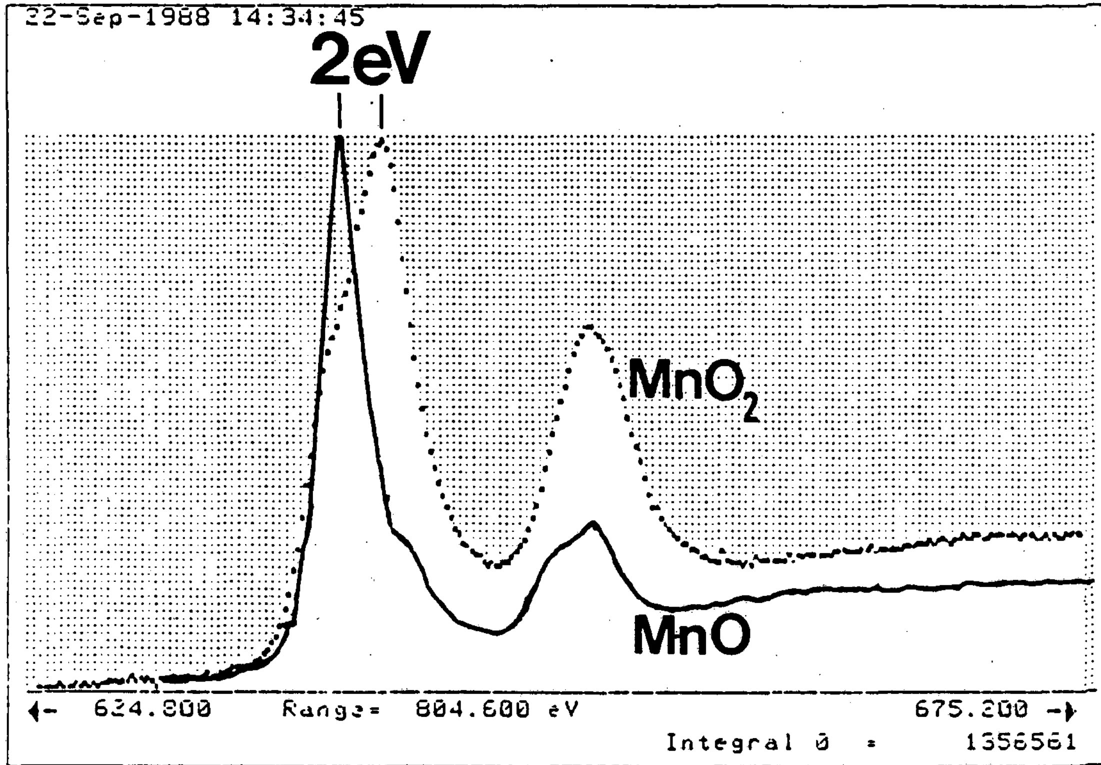

XBL 8810-3586

Figure 4

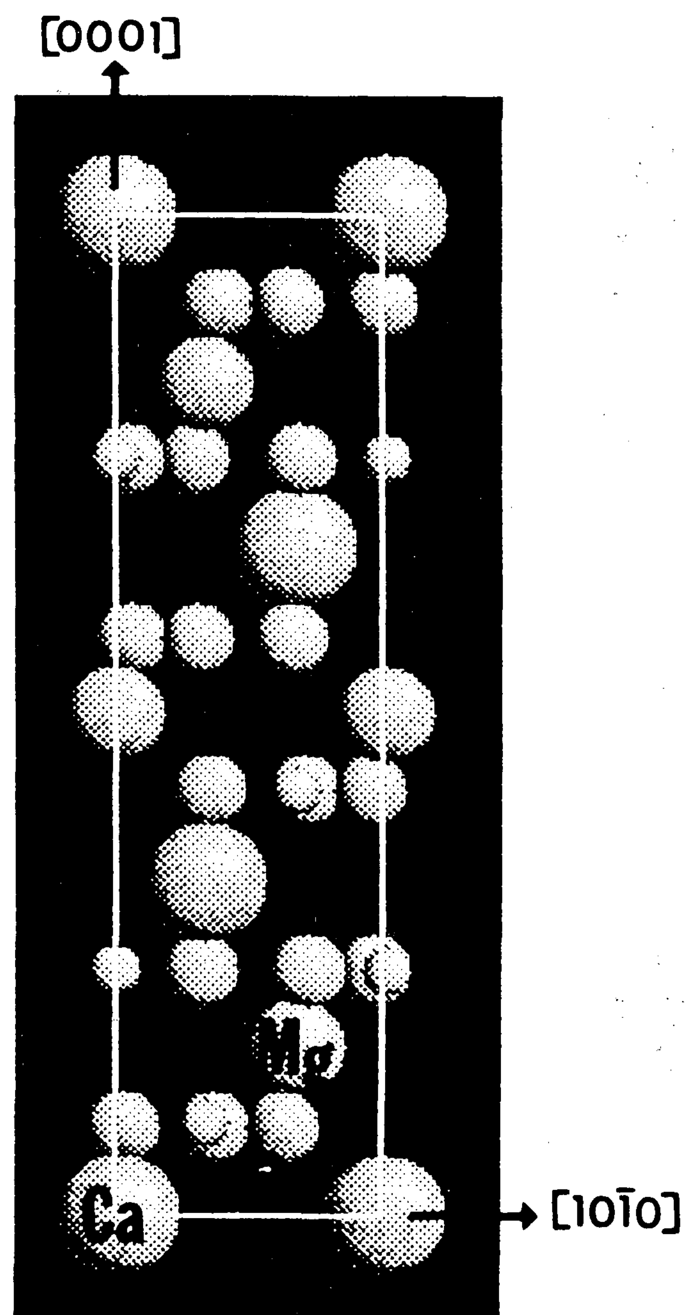

DOLOMITE [1$\bar{2}$10]

XBL 8711-4768 A

Figure 5

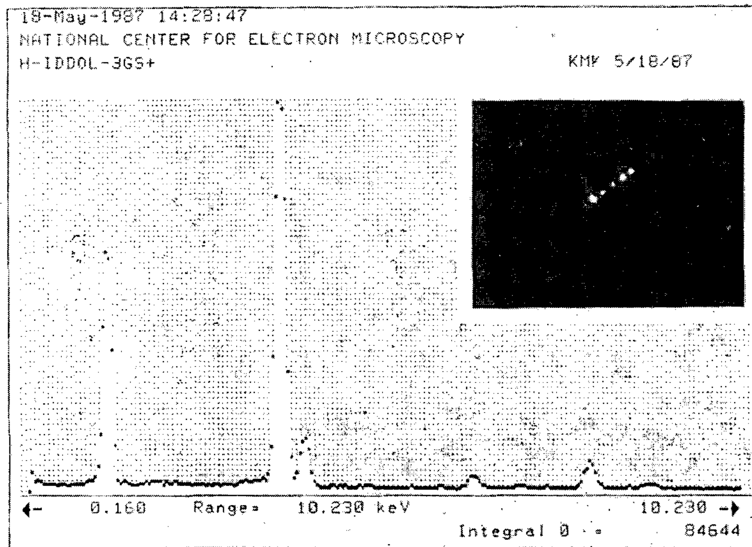

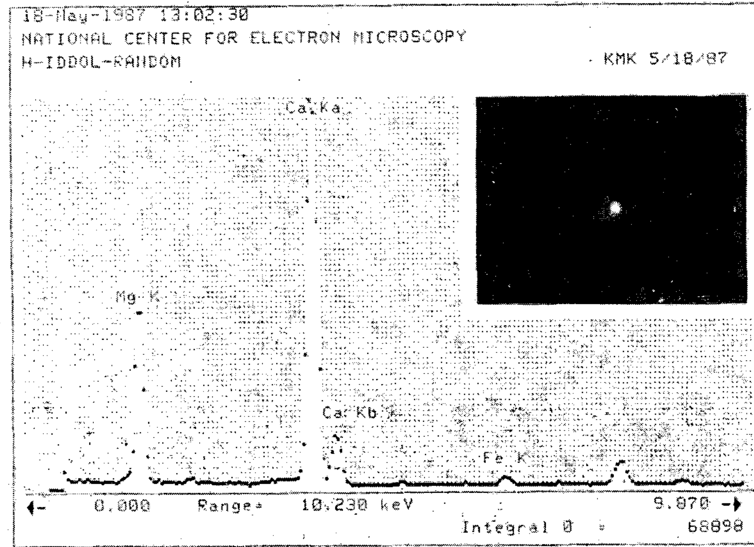

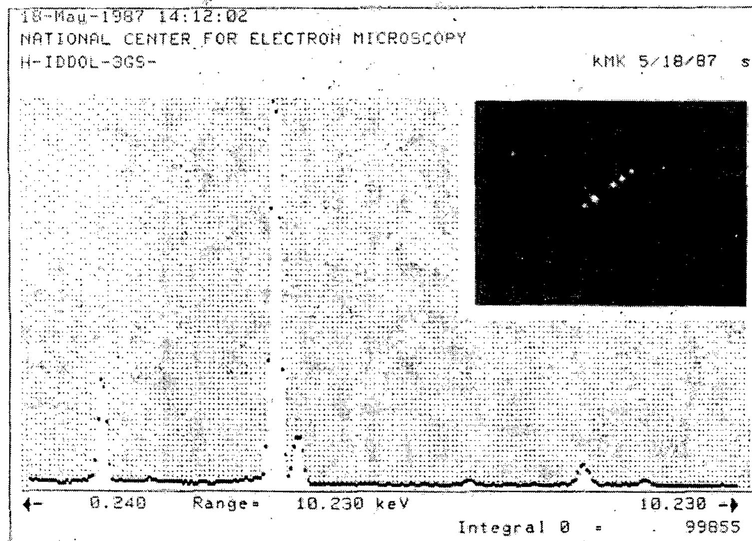

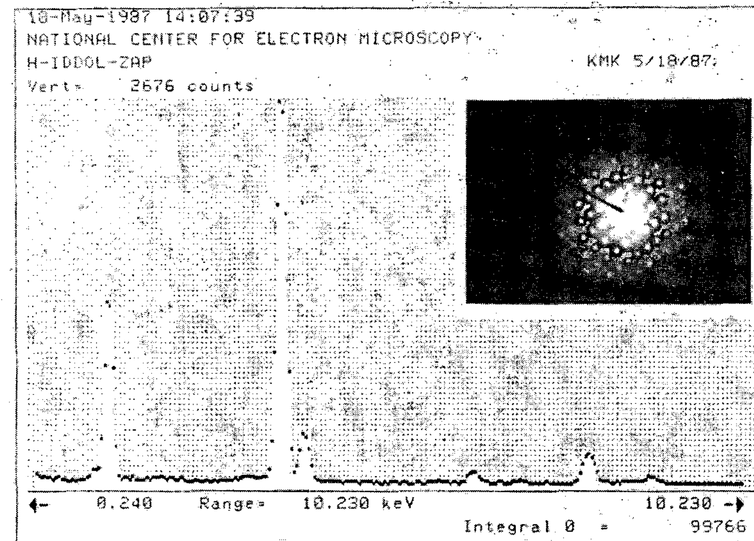

XBB 877-5443

Figure 6

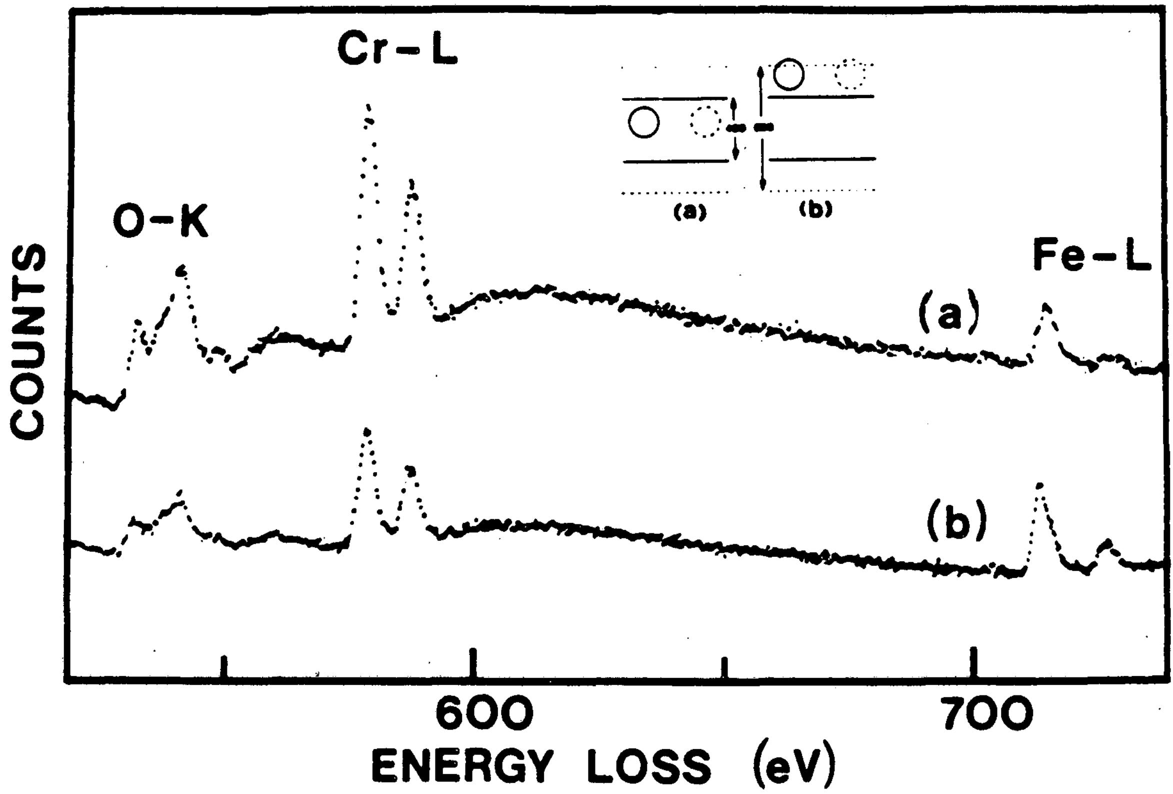

XBL 8610-3781

Figure 7a

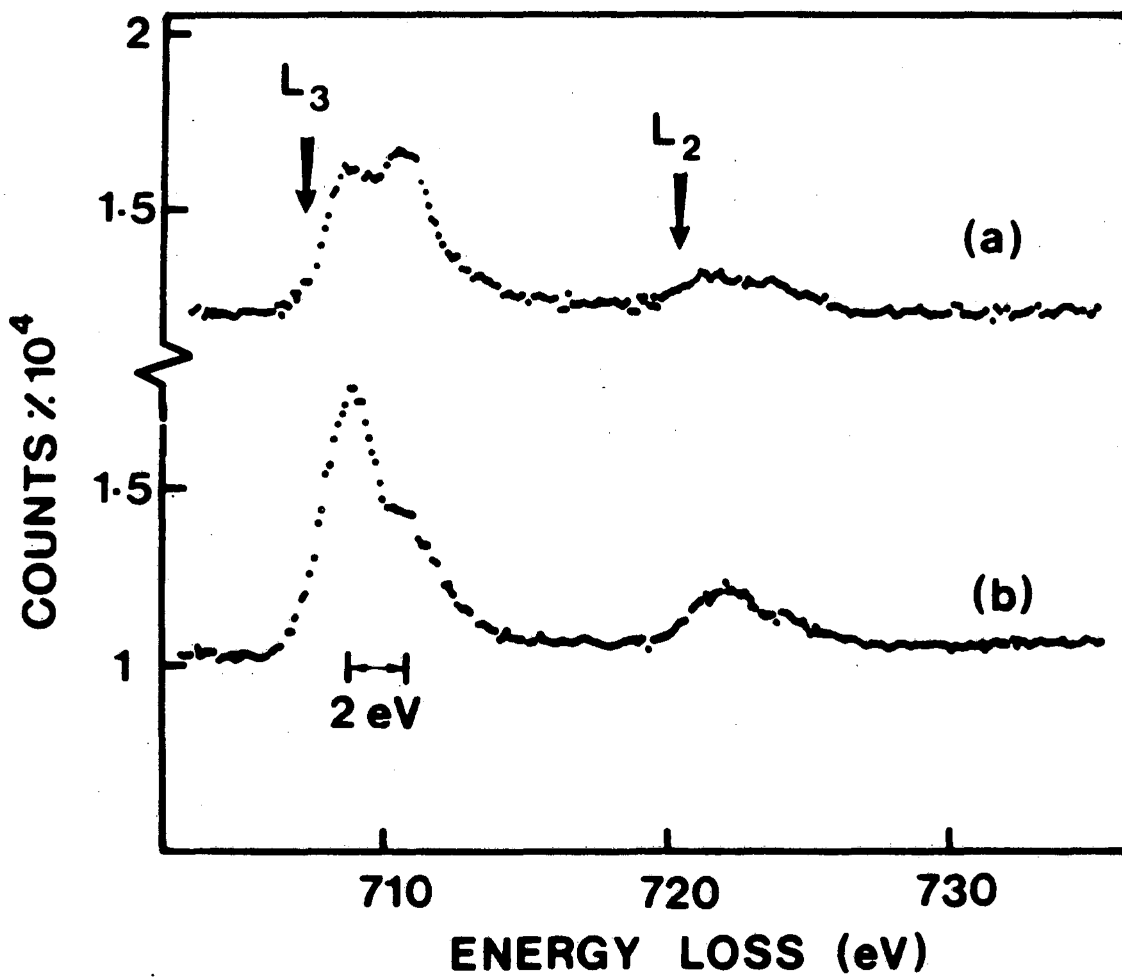

Figure 7b

LAWRENCE BERKELEY LABORATORY
CENTER FOR ADVANCED MATERIALS
1 CYCLOTRON ROAD
BERKELEY, CALIFORNIA 94720